Dynamic Analysis of a High-Bandwidth, Large-Strain, PZT Cellular Muscle Actuator with Layered Strain Amplification

Thomas W. Secord, Jun Ueda, and H. Harry Asada

Abstract— This paper presents the dynamic analysis of an artificial muscle actuator designed for high-bandwidth, power-law strain amplification. The actuator is based on a nested cellular architecture of PZT stack actuators. Most smart material actuators have seen limited use in mobile robotic applications because of their small strain, low stress capacity, low bandwidth, and stringent input requirements. The proposed actuator design overcomes these limitations and can serve as a high-bandwidth multifunctional artificial muscle. The dynamic characteristics of the actuator design are derived analytically and validated experimentally. A test system mimicking flapping flight is then used to illustrate the actuator dynamics.

I. INTRODUCTION

Animals exploit the multi-functional muscle characteristics for energy efficient running, flying, and swimming as well as for adaptive negotiation of varying environments [1]. Traditional DC and AC motors do not have compliance in their inherent physical construction. Rather, external springs and compliant elements must be attached to the electric motors in order to store strain energy and exhibit flexible behavior.

The robotics community has been studying a combination of rigid actuators and springs for nearly four decades. For manipulation, elastic fingers with built-in springs were constructed in the 1970's [2]; Raibert's hopping robots [3] exploited coil springs incorporated into hydraulic cylinders for stable and energy-efficient dynamic locomotion [4]; Cutkosky's cockroach robots were equipped with tuned viscoelastic legs made from a layered manufacturing process [5]. For flying with flapping wings, compliance characteristics of the wing structure or of external springs attached to the robot structure play an important role [6], [7]. In particular, resonance between the wings and the actuators allows for energy efficient flying [7], [15]. A number of effective design concepts have recently been developed in biologically inspired robots [8], [9], [10], [11].

Existing muscle actuator materials (e.g. shape memory alloys, conducting polymers, and dielectric elastomers) are promising for many applications, but they do not possess the high bandwidth, high compliance, high reliability, or high efficiency characteristics required for mimicking biological systems. Piezoelectric actuators such as lead zirconate titanate (PZT) have extremely high bandwidth and high efficiency, which makes them appropriate for mobile

T. Secord, J. Ueda, and H. H. Asada are with the Department of Mechanical Engineering, Massachusetts Institute of Technology, Cambridge, MA, USA {secord,uedajun,asada}@mit.edu .

J. Ueda is also with the Graduate School of Information Science, Nara Institute of Science and Technology, Ikoma, Nara, Japan.

robot applications [6]. The most critical drawback of PZT, however, is its extremely small strain of only 0.1 %. This has limited its application to micro robots and other small load applications. Numerous strain amplifying mechanisms have been presented in the literature, for example [12], [14], but such PZT amplification mechanisms achieve less than 2% strain. Recently, an effective mechanism for amplifying strain has been found that achieves an order of magnitude higher amplification in a compact structure [13]. This new mechanism also provides the compliance that facilitates energetically favorable load interaction.

With the use of a layered strain amplification mechanism, the effective strain of a PZT stack actuator can be exponentially increased, achieving over 20% strain compared to its original body length. This large strain would allow the actuators to be used in the same manner as natural skeletal muscles, which produce approximately 20% strain. Furthermore, the PZT stack actuator has a high bandwidth, large stress capacity, and stable material properties. Combined with the compliant layered strain amplification mechanisms, the high strain actuator has the potential to be used in several robotic designs. The objective of this paper is to analyze and quantify the dynamic performance of the high strain PZT actuator and to explore the possibility of building actuators that can resonate with the load.

II. LAYERED STRAIN AMPLIFICATION DESIGN

Fig. 1 shows the design concept of a hierarchical strain amplification mechanism [13]. The displacement created by PZT stack actuators is increased exponentially with multiple layers of amplification mechanism. The basic unit creating a displacement is a PZT stack actuator packed in a rhombus-shaped strain amplifier. As shown on the top left corner of Fig. 1, the displacement of the PZT stack actuator in the horizontal direction is amplified with this mechanism, resulting in a larger displacement in the vertical direction. This type of amplification is a standard design found in the literature [12], [14].

The unique aspect of the layered design is that several of these PZT units are connected together and then enclosed with a larger rhombus strain amplification mechanism. Furthermore, several of these larger units are then connected together and are placed in an even larger rhombus amplifier. When this process is repeated, the effective strain increases exponentially. Fig. 1 includes three different sizes of the rhombus mechanism, creating a three-layer strain amplifier.

The effective strain is the ratio of output displacement to the original body length in the same output direction. Due
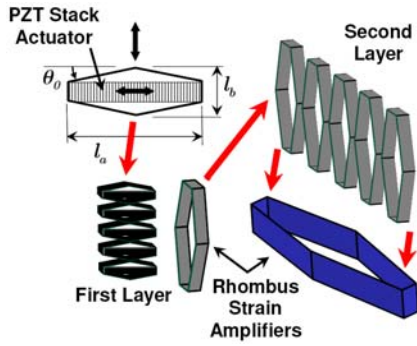
Fig. 1.   Layered architecture of strain amplification devices

to the aspect ratio of the rhombus mechanism, l_a/l_b, shown in Fig. 1, the effective strain amplification is the product of the displacement amplification gain and this aspect ratio. The displacement amplification gain is given by $\cot\theta_0$, where θ_0 is the angle of an oblique edge of the rhombus at a nominal state as shown in Fig. 1. The resultant gain of effective strain amplification g is therefore given by

$$g = \frac{l_a}{l_b}\cot\theta_0. \qquad (1)$$

If each layer has the same value of g and the number of layers is K, then the magnitude and direction of the assembly's effective strain amplification is $(-g)^K$. Considering practical design requirements, a typical value of displacement amplification is $\cot\theta_0 = 5$, while the aspect ratio is typically near 3. If two layers of amplification are used, the effective gain becomes $(5 \times 3)^2 = 225$. Although the strain of PZT is merely 0.1 %, the resultant effective strain of the layered system is over 20%, which is commensurate with the skeletal muscle benchmark.
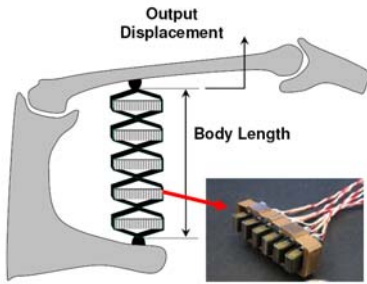

Fig. 2.   Application of a cellular PZT actuator to a skeletal structure

Fig. 2 illustrates a possible biological robot application of this large strain PZT actuator. The artificial muscle shown in the Fig. 2 consists of five stacks of second-layer units. As shown, the cellular architecture allows the PZT actuator to be used in a way similar to the anatomical structure of animal muscles. The following sections address the dynamic modeling and experimental verification of the proposed system, followed by an application to a flapping system.

III. MULTILAYER ACTUATOR DYNAMICS

The dynamics of a fully assembled actuator as shown in Fig. 2 are very complex due to the abundance of closed kinematic chains and unit interconnections. Moreover, several geometric inversions exist within the mechanism that increase the modeling complexity. The scope of this work is to address only the most fundamental subsystem dynamics. This section provides the dynamic analysis of a serial connection of N_2 second layer units as shown in Fig. 3, followed by the analysis of a single unit as a limiting case.

A. Modeling Assumptions

Each rhombus mechanism in the serial connection will be modeled as shown in Fig. 4 (a). The effects of the flexures are lumped into two main torsional stiffnesses k_J and k_B. The stiffness k_J captures the resistance of the flexure joints to rotations in the admissible motion space while the stiffness k_B captures the strain energy storage in the constrained motion space. Thus, the k_B elements allow the oblique beams to store strain energy even with the output displacement of a unit constrained to zero. Each of the stiffnesses can be computed from standard beam theory as

$$k_{J,B} = \frac{Ebt_f^3}{12L_f}, \qquad (2)$$

where E is the elastic modulus of the rhombus material, t_f is the flexure thickness, and L_f is the thickness of the flexure. To further simplify the analysis, the following additional assumptions are used:

- The serial chain of units is constrained to move along a single vertical axis.
- The units in the serial chain are rigidly connected.
- The base rhombus mechanism is grounded to an inertial frame $O-XY$.
- The motion of the rhombus links is symmetric about the vertical and horizontal centerlines.
- The units are identically sized with identical equilibrium configurations quantified by θ_0.
- The thick sections of the rhombus are perfectly rigid.
- The oblique rhombus beams have both mass and rotational inertia.
- The inner first layer units will act as a suspended mass as shown in Fig 4 (b).

The assumption of rhombus symmetry about the centerlines allows each rhombus to be modeled with three generalized coordinates θ_{Ji}, θ_{Bi}, and y_{pi} as shown in Fig 4 (a). The angle θ_{Ji} denotes the excursion of the ith unit's oblique link away from the equilibirium angle θ_0, the angle θ_{Bi} is measured relative to the previous link's position, and the linear distance y_{pi} denotes the position of the ith unit's suspended mass with respect to the local horizontal centerline.

The lumped compliance elements suspending the first layer mass are shown in Fig 4 (b). Notice that the first layer force is introduced using a pure force source f_0 acting in parallel with the compliance k_x.
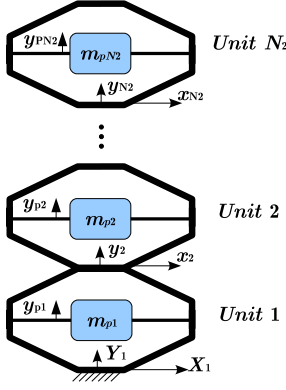
Fig. 3. Dynamic model for a serial connection of a second layer units

(a) Lumped model of a second layer unit

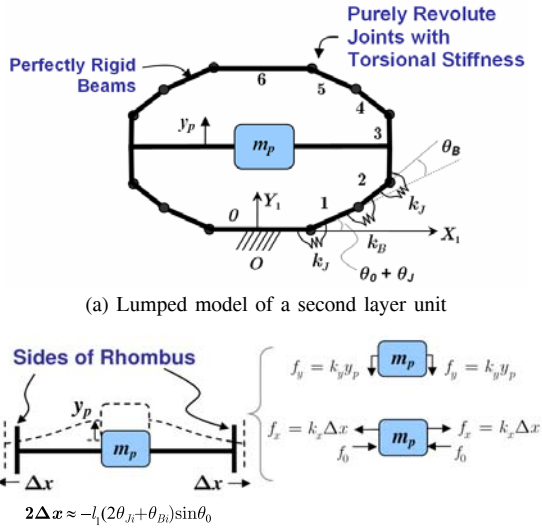(b) Detailed view of suspended lumped mass and compliance elements

Fig. 4. Dynamic lumped parameter model of a second layer unit

The PZT acts a pure force source in parallel with a stiffness k_{pzt}. Assuming linear behavior, the PZT actuator output strain is related to the applied electrical field through the piezoelectric coefficient d_{33}. Strictly speaking, the piezoelecric stiffness and strain coefficent are not constants. However, for simplicity, the following analysis assumes constant PZT parameters. Thus, if the force output of the stack is denoted by f_{pzt}, the output stack displacement is Δx_{pzt}, and the number of films in the stack is N_{film}, then

$$f_{pzt} = k_{pzt}(\beta V - \Delta x_{pzt}), \qquad (3)$$

where $\beta = N_{film} d_{33}$ and V is the applied voltage. From (3), note that the force is a maximum when the displacement is set to zero. This is called the blocking force f_{pzt}^{block} and it corresponds to placing the stack between perfectly rigid supports. Assuming the maximum allowable voltage is applied, then the blocked force is given by $k_{pzt}\beta V_{max}$. Similarly, the displacement under free end conditions is referred to as the the free displacement Δx_{pzt}^{free} and is given

by βV_{max}. With the foregoing definitions of blocked and free conditions, the k_x lumped stiffness may be defined as $k_x = |f_1^{block}|/|\Delta x_1^{free}|$ where the subscript 1 refers to the first layer.

B. Dynamics of Serially Connected Second Layer Units

In the absence of lateral sway, the kinematics of a second layer chain can be determined in terms of the link unit vectors $\hat{\mathbf{e}}_{ij}$. The first subscript $i = 1, 2, ..., N_2$ indicates the unit number as shown in Fig. 3 and the second subscript $j = 0, 1, ..., 6$ indicates the link number as shown in Fig. 4 (a). The general link unit vectors can be written more explicitly as follows:

$$\hat{\mathbf{e}}_{ij} = \begin{cases} \pm\hat{\mathbf{e}}_X & j = 0, 6 \\ \pm\cos(\varphi_i)\hat{\mathbf{e}}_X + \sin(\varphi_i)\hat{\mathbf{e}}_Y & j = 1, 5 \\ \pm\cos(\varphi_i + \theta_{Bi})\hat{\mathbf{e}}_X + \sin(\varphi_i + \theta_{Bi})\hat{\mathbf{e}}_Y & j = 2, 4 \\ \hat{\mathbf{e}}_Y & j = 3 \end{cases}$$

where the $\pm$ are applied sequentially with the associated subscript, $\hat{\mathbf{e}}_{X,Y}$ are the standard cartesian unit vectors aligned with the X and Y axes, and $\varphi_i = \theta_0 + \theta_{Ji}$.

Denoting the length of the jth link as l_j, the linearized velocity of the center of mass of the jth link of unit i ($i \geq 2, j \geq 1$) with respect to the base inertial frame is then given by

$$\mathbf{v}_{Cij} = \sum_{s=1}^{i-1} 2l_1\cos(\theta_0)(2\dot{\theta}_{Js} + \dot{\theta}_{Bs})\hat{\mathbf{e}}_Y$$
$$+ \sum_{r=1}^{j} \tfrac{1}{2}(l_{r-1}\tfrac{d\hat{\mathbf{e}}_{ir-1}}{dt} + l_r\tfrac{d\hat{\mathbf{e}}_{ir}}{dt}). \qquad (4)$$

The three cases not considered in (4) are as follows. When $i = 1$ and $j \geq 1$, the first term in (4) is not present. For the case when $i = 1$ and $j = 0$, $\mathbf{v}_{Cij} = \mathbf{0}$. Finally, for the case when $i \geq 1$ and $j = 0$, $\mathbf{v}_{Cij} = \mathbf{v}_{Ci-1\,6}$.

The rotational kinetic co-energy contained in unit i is

$$T_{rot,i}^* = 2I_{i1}(2\dot{\theta}_{Ji}^2 + \dot{\theta}_{Bi}^2 + 2\dot{\theta}_{Ji}\dot{\theta}_{Bi}) \qquad (5)$$

where I_{i1} is the centroidal mass moment of inertia of link 1, 2, 4, and 5. Given the mass and geometric symmetry assumptions (i.e. $m_0 = m_6$, $l_1 = l_2$, etc.), the total kinetic co-energy of the system can be written

$$T^* = \sum_{i=1}^{N_2} \left(\sum_{j=0}^{6} (m_{ij}\mathbf{v}_{Cij} \cdot \mathbf{v}_{Cij}) \right.$$
$$- \tfrac{1}{2}m_{i0}(\mathbf{v}_{Ci0} \cdot \mathbf{v}_{Ci0} + \mathbf{v}_{Ci6} \cdot \mathbf{v}_{Ci6})$$
$$\left. + T_{rot,i}^* + \tfrac{1}{2}m_{pi}(\dot{y}_{pi} + \mathbf{v}_{Ci2} \cdot \hat{\mathbf{e}}_Y)^2 \right). \qquad (6)$$

The total potential energy contained in the compliant elements is given by

$$V = \sum_{i=1}^{N_2} \left(2k_J\theta_{Ji}^2 + 2k_B\theta_{Bi}^2 + 2k_B(\theta_{Ji} + \theta_{Bi})^2 \right.$$
$$\left. + k_x l_1^2(2\theta_{Ji} + \theta_{Bi})\sin(\theta_0) + k_y y_{pi}^2 \right). \qquad (7)$$

The generalized force acting on the y_{pi} coordinate is identically zero. The generalized forces acting on the angular coordinates are $\Xi_{\theta Ji}$ and $\Xi_{\theta Bi}$:

$$\Xi_{\theta Ji} = -2f_{0i}l_1\sin(\theta_0). \quad (8)$$

and

$$\Xi_{\theta Bi} = -f_{0i}l_1\sin(\theta_0). \quad (9)$$

Defining $\{\xi\} = [\theta_{J1}\ \theta_{B1}\ y_{p1}...\theta_{JN2}\ \theta_{BN2}\ y_{pN2}]^T$ and $\{\Xi\} = [\Xi_{J1}\ \Xi_{B1}\ 0...\Xi_{JN2}\ \Xi_{BN2}\ 0]^T$, the equations of motion are given by Lagrange's equations in standard form:

$$\frac{d}{dt}\left(\frac{\partial \mathcal{L}}{\partial\{\dot{\xi}\}}\right) - \frac{\partial \mathcal{L}}{\partial\{\xi\}} = \{\Xi\}^T, \quad (10)$$

where $\mathcal{L} = T^* - V$ is the difference of (6) and (7). The equations of motion are considered explicitly for the case of a single second layer unit in the following sub-section.

C. Dynamics of a Single Second Layer Unit

The physical actuator prototype shown in Fig. 5 consists of a single second layer unit, which is a limiting case of the dynamics discussed in III-B. Using the second order accurate Lagrangian $\mathcal{L}$, the dynamics of the system are described by the following 3×3 vibratory system:

$$\begin{bmatrix}\mathbf{M}_{3\times 3}\end{bmatrix}\begin{bmatrix}\ddot{\theta}_{J1}\\ \ddot{\theta}_{B1}\\ \ddot{y}_{p1}\end{bmatrix} + \begin{bmatrix}\mathbf{K}_{3\times 3}\end{bmatrix}\begin{bmatrix}\theta_{J1}\\ \theta_{B1}\\ y_{p1}\end{bmatrix} = \begin{bmatrix}\Xi_{\theta J1}\\ \Xi_{\theta B1}\\ 0\end{bmatrix}, \quad (11)$$

where the elements of the mass and stiffness matrices follow from (10).

IV. IMPLEMENTATION AND EXPERIMENT

A. Prototype Construction

A prototype was constructed for experimental investigation. The prototype is shown in Fig. 5 and consists of six first-layer units contained within a bronze outer rhombus, i.e. the second layer strain amplification. All inter-unit and inter-layer connections were made using conventional epoxy.

This prototype design uses a commercially available TF-PZT stack actuator produced by Cedrat, Inc. [18]. This PZT stack has an approximate blocking force of 460 N, a free displacement of 12 μm, and a maximum continuous voltage of 150 V. Along the output axis of the amplification mechanism, this first layer unit produces a free displacement of 80 μm. Thus, when placed in series, the 6 first-layer units have a free displacement of 480 μm. The fully assembled second layer unit was found to have a free displacement output of 2.49 mm, giving an effective strain of approximately 20% compared to the original body length of 13 mm.
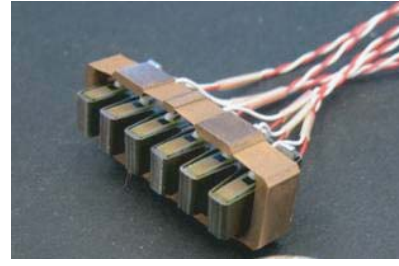

Fig. 5. Physical prototype consisting of 6 serially connected first layer units (Cedrat, Inc.) contained within an outer rhombus

B. Experimental Validation

A frequency response test was performed as a validation of the linear dynamic equations in (11). The transfer function between the link 6 vertical displacement ΔY_6 and the input force $f_0(t)$, denoted by $\Delta Y_6(s)/F_0(s)$, was identified.

The test apparatus shown in Fig. 6 was used to measure the response of the prototype mechanism under fixed-free conditions. The overall construction provides a single rigid constraint that aligns the actuator output axis with the measuring axis of a Micro-Epsilon ILD 1401-10 laser displacement sensor. All data were acquired using a PCI-6036E data acquisition card and LabVIEW^{TM} 7.1. Voltages were applied to the PZT stacks using a Cedrat CA-45 amplifier. For clarity, the PZT stack leads are shown unconnected in Fig. 6.
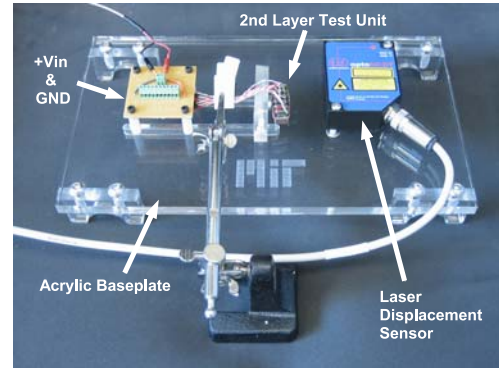

Fig. 6. Test equipment designed for measurement of actuator dynamic performance

A chirp voltage input $V_{in}(t)$ was applied in parallel to the six PZT stacks in the first layer. To assure adequate signal power within the actuator bandwidth, the chirp frequency ranged from 0.3 Hz to 500 Hz, with a peak amplitude value of 30 V and a minimum value of 0 V. The PZT stack input voltage and actuator output displacement were measured using the aforementioned equipment. Under free end conditions, the input stiffness of the 2nd layer rhombus is approximately 0.04 $N/\mu m$. From this stiffness, the input force f_0 is computed to be 3.08 N for an input voltage of 30 V. The force was assumed to vary sinusoidally from 0 to this maximal value; therefore $f_0 \approx 0.103V_{in}$.

TABLE I

PARAMETERS USED IN THEORETICAL MODEL

Parameter	Symbol	Value	Units
Link 0 Mass	m_0	0.0851	g
Link 1 and 2 Mass	m_1	0.173	g
Link 3 Mass	m_3	0.692	g
First Layer Mass	m_p	12	g
Total Actuator Mass	m_T	15	g
Total Length of Oblique Links	l_1	12.9	mm
Flexure Zone Length	L_f	3.51	mm
Flexure Thickness	t_f	0.1	mm
Rhombus Width	b	5.01	mm
Lumped Horizontal Stiffness	k_x	12	N/mm
Lumped Vertical Stifness	k_y	4	N/mm
Link 1 and 2 Inertia	I_1	2.27×10^{-9}	kg $\cdot m^2$
Elastic Modulus	E	110	GPa
Initial Link Angle	θ_0	5	deg

Fig. 7. Theoretical and measured frequency response of a second layer unit

The theoretical transfer function $\Delta Y_6(s)/F_0(s)$ was computed using (11), and the parameters in Table I. In Table I, the lumped vertical stiffness parameter k_y was the only parameter that could not be computed theoretically. It was therefore set based on a linear finite element analysis of six first layer units deflected vertically. The response of the measured system and the theoretical system are plotted together in Fig. 7.

The theoretical mode shapes and natural frequencies were readily obtained by solving the standard eigenvalue problem associated with the matrix $\mathbf{M_{3 \times 3}}^{-1}\mathbf{K_{3 \times 3}}$. The fundamental mode exhibits in phase motion of the piezo unit and the rhombus vertical vibration. The second mode exhibits opposing phase motion of the piezo units of the rhombus. The measured frequencies for these modes were 61.1 Hz and 303 Hz respectively. The corresponding theoretical values were 58.8 Hz and 224.0 Hz. The complex zero frequency of the model resides at 79.4 Hz with the measured value residing at 84.1 Hz. The highest frequency mode in the model resides at 1162.7 Hz, but this mode could not be measured because of the 1 kHz bandwidth of the displacement sensor.

C. Model Competence

The fundamental mode from the model and experiment agree within 4% while the second mode agrees within 26%. These results are independent of the voltage excitation amplitude up to the 30 V maximum amplitude used. The independence of the result from amplitude and the well behaved phase in Fig. 7 indicate that the linear model is competent to describe the dynamics of a second layer unit in the frequency range of interest. Furthermore, the data indicate that the assumed system order and pole-zero topologies are fundamentally correct.

A small disparity between the measured and modeled responses arises due to lack of damping in the model. The high frequency disparity may be due in part to the unmodeled dynamics of the wiring. If the wiring acts as increased stiffness, this would serve to raise the modal frequencies in the real system over the theoretical case. Also, the axial stiffness and mass of the flexures were neglected and the
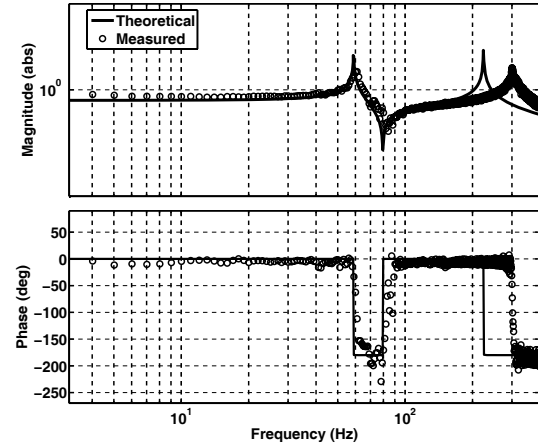
torsional spring approximation introduces some error for the large value of L_f. Another likely cause of high frequency disparity is the uncertainty in the lumped vertical stiffness k_y and the effective lumped piezo mass m_p.

The foregoing validation of the actuator model provides a basis for establishing the closed loop bandwidth or tracking capability. The model can also be readily extended to accurately determine the fundamental mode of the loaded actuator system, which is discussed in the following section.

V. FLAPPING SYSTEM DYNAMICS

The second layer actuator unit was coupled to a flapping system as shown in Fig. 8. Flapping flight involves transient periods of high frequency wing movement, such as in takeoff and landing as well as steady state flapping dynamics at an intermediate frequency. To achieve maximum efficiency, the system should be capable of resonating at various frequencies. This idea is also dicussed in [7] for a hypothetical pigeon sized bird and in [15] for microaerial vehicles. A successful flapping robot requires a design that minimizes weight and produces the appropriate aerodynamic forces. Such design issues are beyond the scope of the test system described here, but complete discussions can be found in [7], [15], [16], [17].
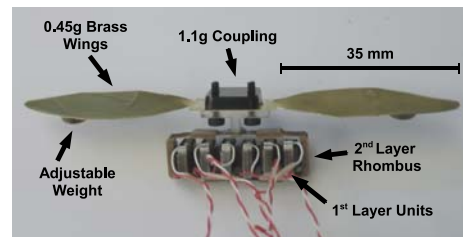

Fig. 8. Flapping system used to illustrate the resonance capabilities of the loaded actuator

A. Extension of the Dynamic Model

The winged system introduces additional vibratory modes to the actuator system. The dynamic model was extended to capture only the fundamental vibration mode of the load. Although it is utilized in most flapping flight robots, the torsional oscillation mode of wings is not included in the extended model. For simplicity, drag forces are also neglected.

Under these assumptions, the dynamic model becomes a 4×4 vibratory system by adding in terms represresting the additional kinetic and potential energy of the wings (m_w = 0.45 g, k_w = 11 N/m) to (6) and (7) respectively and then re-applying (10).

B. Experiments with the Winged System

Using the same voltage chirp and measurement system described in IV-B, the frequency domain response of the winged system was determined. The results of the experiment are shown in Fig. 9 along with the theoretical model results.
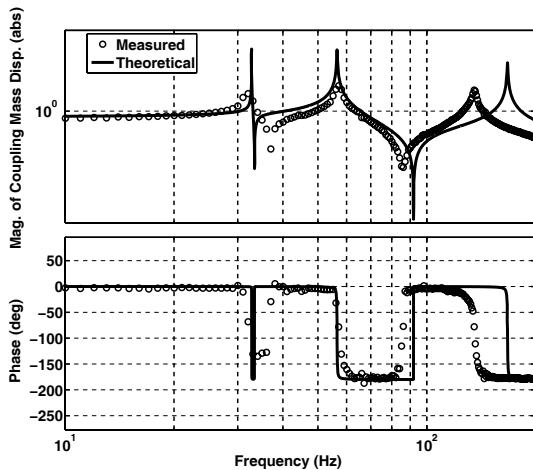
Fig. 9. Measured frequency response of the flapping system coupling mass

The measured first mode frequency was 32.0 Hz with the model predicting 32.8 Hz. The higher frequency modes are also captured with the extended model and show only a moderate discrepancy. The fundamental mode wingbeat frequency is in a reaonable range for dragonfly-sized robots to achieve sufficient lift for flight [15], however the power density of the current design is not sufficient for flight. Overall, the model of the wing dynamics can accurately predict the behavior of the system resonances, which will be very useful in later designs and structural resonance control efforts.

VI. CONCLUSION

This work describes the dynamics of a flexure-based cellular actuator design. The most unique dynamical feature of the proposed actuator design is its ability to mechanically resonate at several frequencies. For N_2 units there are $3N_2$ lightly damped natural frequencies. Maximum power transfer may be achieved by driving the system to one of the resonant peaks or by changing the location of the resonant peaks via configuration changes from the addition of loads.

The specific contributions of this work may be summarized as follows. First, a general cellular PZT design concept has been presented and a second layer unit prototype was constructed. A dynamic model suitable for control and load impedance matching was formulated and analyzed in the frequency domain. The linearized dynamic model showed close agreement with experimental frequency response data. A flapping flight system was constructed to illustrate one possible application of the actuator.

Future work will focus on further prototype development, antagonistic actuator arrangements, and control algorithms for resonance tuning.

REFERENCES

[1] M.H. Dickinson , C.T. Farley , R.J. Full , M.A.R Koehl , R. Kram , and S. Lehman, "How Animals Move", *Science*, Vol. 288, pp. 100-106, 2000.

[2] H. Hanafusa and H. Asada, "A Robotic Hand with Elastic Fingers and Its Application to Assembly Processes", *Proc of FAC Symp. on Information Control Problems in Production Engineering*, pp. 127-138, October 1977.

[3] M. Raibert, "Legged Robots That Balance", MIT Press, April 2000.

[4] R. Ghigliazza, R. Altendorfer, P. Holmes, and D.E. Koditschek, "Passively Stable Conservative Locomotion", *SIAM J. on App. Dynamical Systems*, Vol. 2, No. 2,pp. 187-218, 2003.

[5] J.G. Cham, S.A. Bailey, J.E. Clark, R.J. Full, and M.R. Cutkosky, "Fast and Robust Hexapedal Robots via Shape Depostition Manufacturing", *Int. J. of Robotics Research*, Vol. 21, Issue 10, 2002.

[6] J. Yan, M. Dickinson, J. Birch, M. Sitti, T. Su, and R. Fearing, "Wing Transmission for a Micro-Mechanical Flying Insect", *J. of Mircomechatronics*, Vol. 1, No. 3, pp. 221-237, 2002.

[7] K.K. Issac and S.K. Agrawal, "An Investigation Into the Use of Springs and Wing Motions to Minimize the Power Expended by a Pigeon-Sized Mechanical Bird for Steady Flight", *J. Mech. Design*, Vol. 129, pp. 381-389, 2007.

[8] D.L. Alshuler, R. Dudley, and C.P. Ellington, "Aerodynamics Forces of Revolving Hummingbird Wings and Wing Models", *J. Zoology*, London, Vol. 264, pp. 327-332, 2004.

[9] S. Frazier et. al., "Elasticity and Movements of Cockroach Tarsus in Walking", *J. Comp. Physiology A*, Vol. 185, No. 2, pp. 157-172.

[10] K. Daltorio, A. Horchler, S. Gorb, R. Ritzmann, and R. Quinn, "A Small Wall-Walking Robot with Compliant, Adhesive Feet, *Proc. of IEEE/RSJ Int. Conf. on Robots and Systems*, Edmonton, Canada, 2005.

[11] J. Toomey and J. Eldredge Numerical and Experimental Investigation of the Role of Flexibility in Flapping Wing Flight, *AIAA Fluid Dynamics Conference and Exhibit*, pp. 2006-3211, 2006.

[12] A. Dogan, K. Unchino, R.E. Newnham, "Composite Piezoelectric Transducer with Truncated Conical Endcaps, Cymbal", *IEEE Transactions on Ultrasonics, Ferroelectrics, and Frequency Control*, Vol. 44, pp. 597-605, 1997.

[13] J. Ueda, T. Secord, and H. Asada, "Design of PZT Cellular Actuators with Power-law Strain Amplification", Accepted for Publication in *Proc. of IEEE/RSJ Int. Conf. on Robots and Systems*, San Diego, CA, 2007.

[14] P. Jänker, M. Christmann, F. Hermle, T. Lorkowski, and S. Storm, "Mechatronics Using Piezoelectric Actuators", *J. of the European Ceramic Society*, Vol. 19, pp. 1127-1131, 1999.

[15] A. Cox, E. Garcia, and M. Goldfarb, "Actuator Development for a Flapping Microrobotic Mircoaerial Vehicle", *Proc. of SPIE Conf. on Microrobotics and Micromanipulation*, Vol. 3519, pp. 102-108, 1998.

[16] J. Yan, R.J. Wood, S. Avandhanula, M. Sitti, and R.S. Fearing, "Towards Flapping Wing Control for a Micromechanical Flying Insect", *Proc. of IEEE Int. Conf. on Robotics and Automation*, Seoul, Korea, pp. 3901-3908, 2001.

[17] N. Vandenberghe, S. Childress, and J. Zhang, "On Unidirectional Flight of a Free Flapping Wing," *Physics of Fluids*, Vol. 18, pp. 014102-014102-8, 2006.

[18] CEDRAT Inc., http://www.cedrat.com/.